

## Rapidly Intensifying Hurricane Guillermo (1997). Part II: Resilience in Shear

PAUL D. REASOR

*Hurricane Research Division, NOAA/AOML, Miami, Florida*

MATTHEW D. EASTIN

*Department of Geography and Earth Sciences, University of North Carolina at Charlotte, Charlotte, North Carolina*

(Manuscript received 30 March 2011, in final form 13 July 2011)

### ABSTRACT

This paper examines the structure and evolution of a mature tropical cyclone in vertical wind shear (VWS) using airborne Doppler radar observations of Hurricane Guillermo (1997). In Part I, the modulation of eyewall convection via the rotation of vorticity asymmetries through the downshear-left quadrant was documented during rapid intensification. Here, the focus is on the relationship between VWS, vortex tilt, and associated asymmetry within the tropical cyclone core region during two separate observation periods. A method for estimating local VWS and vortex tilt from radar datasets is further developed, and the resulting vertical structure and its evolution are subjected to statistical confidence tests. Guillermo was a highly resilient vortex, evidenced by its small tilt magnitude relative to the horizontal scale of the vortex core. The deep-layer tilt was statistically significant, oriented on average  $\sim 60^\circ$  left of shear. Large-scale vorticity and thermal asymmetries oriented along the tilt direction support a response of Guillermo to shear forcing that is consistent with balanced dynamics. The time-averaged vertical motion asymmetry within the eyewall exhibited maximum ascent values  $\sim 40^\circ$  left of the deep-layer shear, or in this case, right of the deep-layer tilt. The observation-based analysis of Guillermo's interaction with VWS confirms findings of recent theoretical and numerical studies, and serves as the basis for a more comprehensive investigation of VWS and tropical cyclone intensity change using a recently constructed multistorm database of Doppler radar analyses.

### 1. Introduction

Vertical wind shear (VWS) impacts tropical cyclone (TC) structure directly through vertical tilting of the vortex wind field and indirectly through modulation of the convective field. The impact of VWS on TC intensity is less certain and depends, in part, upon the time scale over which one considers the response (Frank and Ritchie 2001; Wang et al. 2004; Wong and Chan 2004; Riemer et al. (2010, hereafter RMN10). The view of VWS as a generally negative influence on TC formation and intensification is supported by observational studies (e.g., Gray 1968; Merrill 1988; DeMaria 1996) and observation-based statistical models of intensity prediction (Kaplan and DeMaria 2003; DeMaria et al. 2005). During the early stages of TC development, however, VWS can play a potentially positive role by organizing

deep convection and vorticity production in the downshear region of the weak, preexisting vortex (Molinari et al. 2004, 2006).

Early studies of the mechanisms for shear-induced intensity change focused on the role of VWS in ventilating the warm core (Simpson and Riehl 1958). Frank and Ritchie (2001) simulated the development of pronounced convective asymmetry in a vertically sheared TC and argued that weakening occurs through the hydrostatic response to outward fluxes of upper-level potential vorticity (PV) and equivalent potential temperature. An alternative explanation by DeMaria (1996) focused on the balanced-dynamical response of the vortex to vertical tilting. To maintain thermal wind balance as the wind structure is tilted, static stability must increase at low levels in the eyewall region. The negative impact on intensity was then hypothesized to arise through suppression of eyewall convection. Using a multilevel adiabatic primitive equation model, Jones (1995, 2000) demonstrated that low-level static stability evolves in a manner consistent with balanced dynamics, but does so asymmetrically within the

---

*Corresponding author address:* Paul D. Reasor, Hurricane Research Division, NOAA/AOML, Miami, FL 33149.  
E-mail: paul.reasor@noaa.gov

eyewall, with anomalously low (high) values located downtilt (uptilt). Thus, while convection might be suppressed on one side of the eyewall, it can be enhanced on the other. Jones additionally implicated the asymmetric transverse circulation of the vertically sheared vortex in the development of convective asymmetry in the eyewall. The net impact of such static stability and vertical motion asymmetry on intensity change remains unclear. Recently, RMN10 have proposed an intensity modification mechanism also rooted in a balanced-dynamical framework. They argued that balanced vorticity asymmetry associated with the vertically tilted vortex at low levels organizes convection outside the eyewall through Ekman pumping. In their simulations, this enhancement of convection led to the transport of low equivalent potential temperature air into the inflow layer and disruption of the TC heat engine (Emanuel 1986, 1991).

In the various theories relating VWS and TC intensity, the vertically coherent state of the vortex would arguably be the one best able to counter the negative impacts of shear. The ability of strong TCs to resist the tendency to tilt when experiencing differential advection by VWS suggests an intrinsic mechanism for vortex resilience. Jones (1995) argued that coupling between the upper- and low-level cyclonic PV anomalies of a sheared vortex can counter the differential advection. The strength of the coupling, and hence the vortex resilience, is enhanced by increasing the local Rossby penetration depth. The factors that increase the penetration depth include reduced static stability, increased horizontal vortex scale, increased vortex strength, and increased Coriolis parameter. Through a regression analysis of Atlantic basin hurricane data, DeMaria (1996) identified the latter three factors as contributing to a reduced sensitivity of hurricanes to the effects of VWS.

Reasor and Montgomery (2001) presented a new paradigm for the adiabatic resilience of TC-like vortices in which the vortex tilt is viewed as an asymmetric perturbation, and the vortex dynamics is approximately linear. In their small Rossby number analysis, the asymmetry associated with unidirectional tilting projected onto vortex Rossby waves (VRWs) having baroclinic vertical structure dominated by azimuthal wavenumber 1. Depending on the Rossby deformation radius of the flow and radial vortex structure, the VRWs were usefully characterized as either quasi modes or sheared spiral structures. The azimuthal propagation of the quasi mode caused precession of the tilted vortex, and its decay was associated with tilt reduction (i.e., vertical alignment). Schecter et al. (2002) provided a formal theory for the tilt quasi mode by separating the vortex into a core with the highest

vorticity and a surrounding skirt of much weaker vorticity.<sup>1</sup> The quasi mode was then represented as an azimuthally propagating discrete VRW with peak amplitude near the transition between core and skirt. The resonant interaction of this discrete core VRW within a critical layer located in the vortex skirt generally yields damping of the vortex tilt for realistic TC wind profiles (e.g., Mallen et al. 2005). In an extension of the adiabatic theory to rapidly rotating vortices in VWS, Reasor et al. (2004, hereafter RMG04) observed that the shear-forced tilt asymmetry exhibited a damped oscillatory behavior in time. A heuristic model of the TC-like vortex in unidirectional shear, which approximates the tilt evolution using a forced-damped oscillator equation, predicted a steady-state tilt with height 90° left of shear for initially *barotropic* vortices.

In Reasor et al. (2009, hereafter Part I) we documented the basic structural and short-time-scale intensity evolution of Hurricane Guillermo (1997), which experienced persistent VWS during a period of rapid intensification. In particular, the core region exhibited a pronounced convective asymmetry, consistently maximized in the downshear-left quadrant of the eyewall. Such a relationship between the direction of deep-layer VWS and eyewall convection is a common feature both of observed (e.g., Reasor et al. 2000; Black et al. 2002; Corbosiero and Molinari 2003; Eastin et al. 2005) and simulated (e.g., Wang and Holland 1996; Bender 1997; Frank and Ritchie 2001; Rogers et al. 2003; Braun and Wu 2007; Davis et al. 2008) TCs constrained by their interaction with shear.

In this part we focus on the interaction of Hurricane Guillermo with the environmental flow, documenting the structure and evolution of VWS, vortex tilt, and related asymmetries within the core region. The dataset is extended here to include radar analyses from a second period when the storm had reached steady-state intensity. In section 2, we discuss the Doppler radar data and methodology for estimating VWS and vortex tilt from radar analyses. The structure and evolution of Guillermo's tilt and related asymmetries in the kinematic and available thermodynamic fields presented in section 3 are consistent with a balanced-dynamical response of the TC to VWS. Conclusions and plans to extend the present analysis to a multicase database of Doppler-observed TCs are discussed in section 4.

---

<sup>1</sup> We will follow this dynamically motivated nomenclature here, but refer to the region encompassing the core and immediate surrounding skirt as the "core region."

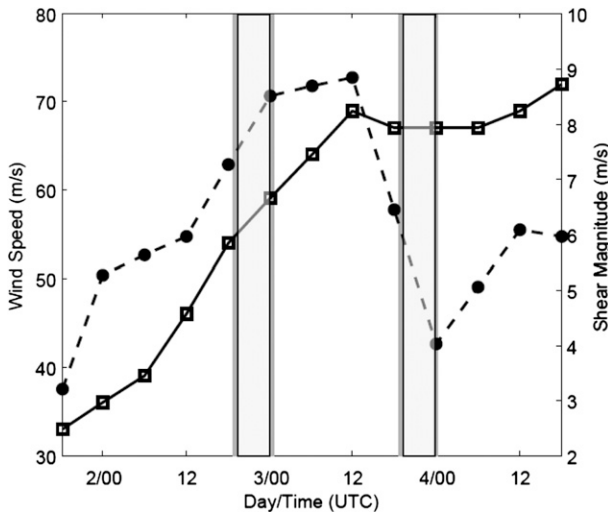


FIG. 1. Official best-track 6-hourly intensity (solid) and SHIPS database 850–200-hPa vertical shear (dashed; DeMaria et al. 2005) estimates for Hurricane Guillermo beginning at 1800 UTC 1 Aug 1997 when it was first declared a hurricane. The 12-hourly vertical shear values have been interpolated to 0600 and 1800 UTC. The gray boxes indicate the approximate Doppler radar analysis periods, referred to here as IOP1 and IOP2.

## 2. A Doppler-based methodology for estimating TC center tilt and local VWS

### a. Synoptic overview of Hurricane Guillermo: 2–4 August 1997

In Part I we documented the structure and evolution of eastern Pacific Hurricane Guillermo (1997) on 2 August during a period of rapid intensification, henceforth referred to as the first intensive observing period (IOP1), using coordinated observations from two National Oceanic and Atmospheric Administration (NOAA) WP-3D Orion aircraft (referred to here as N42RF and N43RF). In this second part, observations are included from a second set of flights on 3 August, referred to as IOP2, approximately 24 h after the start of IOP1. Figure 1 shows the best-track maximum 1-min-sustained 10-m wind speed for Guillermo following hurricane classification at 1800 UTC 1 August (Lawrence 1999). From 1200 UTC 3 August to 1200 UTC 4 August, spanning IOP2, the storm intensity was approximately steady state. The complete dataset utilized here provides a unique opportunity to contrast the vortex structure and evolution during two distinct phases of the TC life cycle.

Overall, the synoptic environment of Guillermo changed little between IOP1 and IOP2. Under the influence of a ridge to its north, Guillermo's west-northwestward speed increased from an average value of  $4.5$  to  $5.5 \text{ m s}^{-1}$ . Sea surface temperatures along the storm's path remained above  $29^\circ\text{C}$  (Reynolds and Smith 1993). The 850–200-hPa

VWS (Fig. 1) was taken from the Statistical Hurricane Intensity Prediction Scheme (SHIPS) database (DeMaria et al. 2005). Although an updated estimate is used here in which the vortex has been removed following Knaff et al. (2011), the basic magnitude and direction remain consistent with the values reported in Part I. This new measure of large-scale VWS is derived from the National Centers for Environmental Prediction (NCEP) operational global model analysis and defined as the vector difference of the mean winds within a 500-km radius of the storm center between 200 and 850 hPa. Between observation periods the VWS fluctuated about the southward-pointing direction, decreasing in magnitude from approximately  $8.5$  to  $4 \text{ m s}^{-1}$ . Interestingly, the rapid intensification period coincided with increasing deep-layer VWS, while the transition to steady-state intensity coincided with a decrease in magnitude. An examination of the corresponding 850–500-hPa shear (not shown) revealed magnitudes consistently less than  $2 \text{ m s}^{-1}$ . Thus, the bulk of the large-scale VWS was concentrated above 500 hPa ( $\sim 5$ – $6 \text{ km}$ ).

### b. Radar observations

Both N42RF and N43RF were equipped with C band (5.5-cm wavelength) lower-fuselage radars and X-band (3.2-cm wavelength) tail Doppler radars (Jorgensen 1984). Table 1 summarizes the aircraft eyewall passes and the approximate Doppler radar compositing period for each. The sampling strategy for IOP1 and IOP2 was similar, with N43RF employing the fore/aft scanning technique (FAST) and N42RF scanning in the track-normal plane (Gamache et al. 1995) during periods of simultaneous measurement.

We refer the reader to Part I for a thorough discussion of the data quality and Doppler analysis method. Briefly, following the application of navigation corrections, standard procedures were employed to remove spurious echoes (e.g., sea clutter) and to dealias the Doppler radial winds. The manually edited fields were then interpolated to a storm-centered 120 km by 120 km Cartesian domain extending from the surface to 20-km altitude with horizontal and vertical grid spacing of 2 and 1 km, respectively. A variational method (Gamache 1997; Part I) was then used to simultaneously solve the Doppler radar projection equations and anelastic mass continuity equation for the three-dimensional wind field. The analysis here is limited to the region between 1 and 10 km as a result of data quality issues affecting estimates of vortex-scale quantities (e.g., vortex tilt) outside this layer.

The quality of the Doppler-retrieved winds for IOP2 was assessed through a comparison with aircraft flight-level measurements following the methodology described in Part I. Table 2 lists the mean difference (i.e., bias),

TABLE 1. Composite period and approximate aircraft inbound locations with respect to the storm center for each pass through Hurricane Guillermo (1997). The Doppler-scanning technique employed by each aircraft is also indicated.

| Pass | Date    | Composite time (UTC) | Aircraft    | Scanning    | Inbound location |
|------|---------|----------------------|-------------|-------------|------------------|
| 1    | 2 Aug   | 1845–1905            | N42RF/N43RF | Normal/FAST | E/N              |
|      | 3 Aug   | 1901–1921            |             |             |                  |
| 2    | 2 Aug   | 1925–1944            | N42RF/N43RF | Normal/FAST | S/E              |
|      | 3 Aug   | 1937–1957            |             |             |                  |
| 3    | 2 Aug   | 1953–2010            | N42RF       | FAST        | NNW              |
|      | 3 Aug   | 2008–2027            |             |             |                  |
| 4    | 2 Aug   | 2033–2052            | N42RF       | FAST        | NE               |
|      | 3 Aug   | 2045–2104            |             |             |                  |
| 5    | 2 Aug   | 2106–2129            | N42RF/N43RF | Normal/FAST | SE/SW            |
|      | 3 Aug   | 2117–2135            |             |             |                  |
| 6    | 2 Aug   | 2144–2158            | N42RF/N43RF | Normal/FAST | SW/NW            |
|      | 3 Aug   | 2154–2213            |             |             |                  |
| 7    | 2 Aug   | 2215–2234            | N42RF       | FAST        | NNE              |
|      | 3 Aug   | 2221–2241            |             |             |                  |
| 8    | 2 Aug   | 2249–2307            | N42RF       | FAST        | SE               |
|      | 3 Aug   | 2258–2316            |             |             |                  |
| 9    | 2 Aug   | 2324–2341            | N42RF/N43RF | Normal/FAST | SW/SE            |
|      | 3–4 Aug | 2337–0000            |             |             |                  |
| 10   | 2–3 Aug | 2354–0012            | N42RF/N43RF | Normal/FAST | NW/SW            |

RMS difference, and linear correlation coefficient for the Cartesian and polar wind components. Overall, the statistics agree well between the two observation periods (cf. Table 2 of Part I). The greatest errors in the horizontal wind components continue to be found within the eye where the synthesis method effectively linearly interpolates wind values in the absence of reflectors. The Doppler analysis will therefore tend to overestimate horizontal wind speeds in the eyes of strong, intensifying hurricanes, which have a tangential wind profile

that is typically U shaped (Kossin and Eastin 2001; Mallen et al. 2005).

Time-averaged reflectivity from the tail radar during IOP1 and IOP2 is shown in Fig. 2 to highlight the quasi-steady impact of VWS on Guillermo's convective structure. The size of the vortex core, as inferred from the radial scale of maximum reflectivity, contracted between IOP1 and IOP2. Such contraction was also evident in the kinematic field with the 2-km radius of maximum symmetric tangential wind (RMW) decreasing from 30 to

TABLE 2. Mean differences (bias), RMS differences, and linear correlation coefficients between aircraft flight-level and Doppler-derived wind components for all data points as well as selected stratifications during the Doppler observation period on 3 Aug. Included is the total number of data points within each region/stratification. A positive (negative) bias indicates the Doppler-derived wind is more positive (more negative) than the flight-level wind.  $V_R$ : radial velocity;  $V_T$ : tangential velocity.

| Parameter | Statistic                        | All   | 3 km  | 6 km  | Eye   | Eyewall | Eye observed | Eye interpolated |
|-----------|----------------------------------|-------|-------|-------|-------|---------|--------------|------------------|
| $U$       | No. of data points               | 1600  | 1029  | 571   | 511   | 1089    | 234          | 277              |
|           | Mean error ( $\text{m s}^{-1}$ ) | −0.01 | 0.10  | −0.20 | −0.29 | 0.12    | −0.17        | −0.40            |
|           | RMSE ( $\text{m s}^{-1}$ )       | 3.45  | 3.01  | 4.13  | 4.91  | 2.39    | 4.06         | 5.68             |
|           | Correlation                      | 0.99  | 0.99  | 0.99  | 0.98  | 0.99    | 0.99         | 0.97             |
| $V$       | Mean error ( $\text{m s}^{-1}$ ) | −0.30 | −0.33 | −0.24 | −0.54 | −0.19   | −0.65        | −0.44            |
|           | RMSE ( $\text{m s}^{-1}$ )       | 3.39  | 2.94  | 4.09  | 4.33  | 2.34    | 4.13         | 4.82             |
|           | Correlation                      | 0.99  | 0.99  | 0.99  | 0.98  | 0.99    | 0.99         | 0.97             |
|           |                                  |       |       |       |       |         |              |                  |
| $W$       | Mean error ( $\text{m s}^{-1}$ ) | 0.11  | 0.18  | −0.02 | 0.89  | −0.26   | 0.77         | 0.98             |
|           | RMSE ( $\text{m s}^{-1}$ )       | 1.76  | 1.55  | 2.08  | 1.57  | 1.84    | 1.71         | 1.45             |
|           | Correlation                      | 0.57  | 0.58  | 0.54  | 0.16  | 0.57    | 0.25         | 0.12             |
|           |                                  |       |       |       |       |         |              |                  |
| $V_R$     | Mean error ( $\text{m s}^{-1}$ ) | −0.11 | −0.29 | 0.25  | 0.08  | −0.36   | 0.56         | −0.34            |
|           | RMSE ( $\text{m s}^{-1}$ )       | 2.68  | 2.63  | 2.75  | 2.95  | 2.54    | 2.96         | 2.94             |
|           | Correlation                      | 0.85  | 0.89  | 0.71  | 0.62  | 0.89    | 0.71         | 0.51             |
|           |                                  |       |       |       |       |         |              |                  |
| $V_T$     | Mean error ( $\text{m s}^{-1}$ ) | 1.44  | 0.87  | 2.07  | 4.49  | 0.06    | 2.76         | 5.77             |
|           | RMSE ( $\text{m s}^{-1}$ )       | 3.46  | 2.72  | 4.58  | 5.67  | 1.56    | 4.42         | 6.37             |
|           | Correlation                      | 0.99  | 0.99  | 0.98  | 0.97  | 0.98    | 0.98         | 0.96             |
|           |                                  |       |       |       |       |         |              |                  |

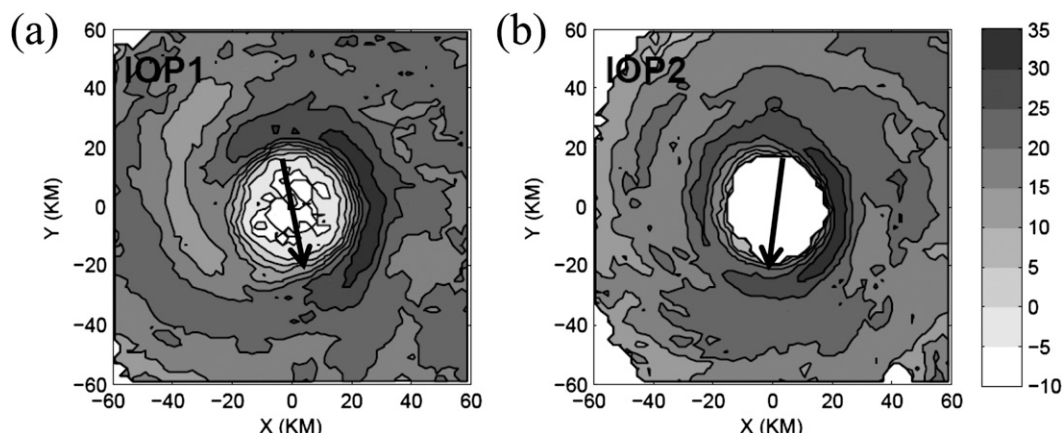


FIG. 2. Time-averaged reflectivity (dBZ) from the tail radar analyses at 3 km during (a) IOP1 and (b) IOP2. Maximum values are located left of the southward-pointing SHIPS deep-layer shear vector.

26 km. During IOP1 the eyewall reflectivity exhibited a pronounced asymmetry with the largest values confined to the left-of-shear semicircle. The eyewall reflectivity during IOP2 was considerably more symmetric, perhaps a consequence of faster advective speeds and weaker VWS, but still with maximum values biased to the left of shear. The open eyewall structure and connecting band observed on the western side during IOP1 was mostly absent 24 h later when Guillermo had reached steady-state intensity. The location of the eyewall reflectivity maximum is consistent with the downwind advection of hydrometeors from a downshear to downshear-left maximum in convection (see Figs. 7 and 17 in Part I).

### c. Quantification of TC center tilt

When a vertically coherent vortex is exposed to VWS, differential advection tends to cause a lateral displacement of the PV anomaly at any given altitude relative to the surface PV anomaly. The resulting tilted vortex structure differs from that expected of passive advection, however, due to the elastic nature and vertical coupling of the vortex (Jones 1995; RMG04). One means of quantifying the magnitude of cyclonic vortex tilt is to measure the lateral displacement of the local pressure (geopotential) minimum at each altitude (pressure level) relative to the surface minimum location. In dry numerical simulations this measure generally provides a robust measure of the vortex core tilt (e.g., Jones 1995). An alternative measure replaces the local pressure minimum with the local (potential) vorticity maximum. As discussed by Jones (1995), this measure tends to be more sensitive to meso-scale details of the vortex flow. In moist numerical simulations of TCs, and presumably observed TCs, neither of the above measures may yield an adequate estimate of the vortex core center when intense mesocyclones are present within the eyewall region. Such center estimates

will be skewed toward the orbiting local pressure minimum and PV maximum of the mesocyclone.

Local measures of center based upon maximum or minimum properties of the vortex core can produce potentially misleading conclusions regarding the interaction of the TC with VWS. When the (potential) vorticity centroid is used instead to define vortex center and vortex tilt, both dry and moist numerical simulations of TC-like vortices in VWS reveal a dependence of vortex tilt on spatial scale (Jones 1995; RMG04; Jones 2004; RMN10). The centroid computed on the eyewall scale and smaller can exhibit significantly less vertical variation than the centroid computed within a radial domain of  $2\text{--}3 \times \text{RMW}$ . When the vortex tilt is viewed from the linear perspective of RMG04, this spatial dependence is accounted for by the radial structure of the shear-forced quasi mode (see their Fig. 13b). Although the vorticity of the mode peaks near the transition from core to skirt, the presence of the vortex skirt allows the asymmetry to extend well outside the core. It is possible therefore for the vortex inside the RMW to exhibit little vertical tilt (relative to the horizontal vortex scale), while the larger-scale vortex exhibits a significant structural response to shear forcing.

The nature of the Doppler-derived wind field in mature TCs limits the application of kinematically based center-finding approaches. Sparsely distributed reflectors within the eye prohibit an accurate assessment of local measures of center like circulation minimum or vorticity maximum. The standard method for estimating the TC center from Doppler radar analyses, described in Part I, seeks to maximize the symmetric component of tangential wind on the RMW scale (Marks et al. 1992; hereafter, referred to as the “MHG method”). The center-finding algorithm specifies an annulus of fixed width  $\delta$ , centered on a vertically varying initial-guess RMW. At each altitude the annulus is given small displacements about the initial-guess



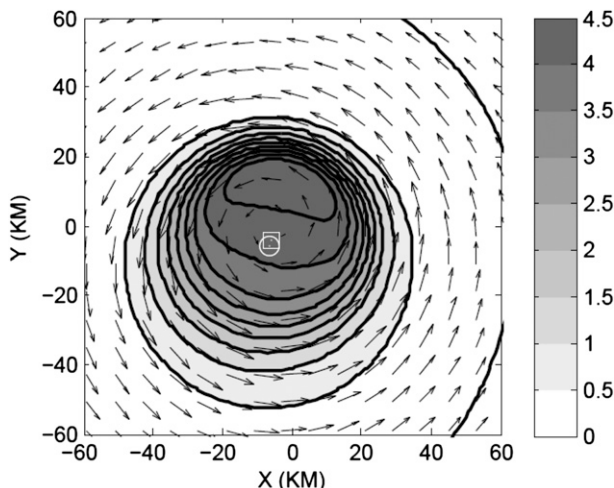


FIG. 3. Earth-relative wind (vectors) and vorticity (shaded,  $10^{-3} \text{ s}^{-1}$ ) fields at the lowest level of a simulated dry Guillermo-like vortex in westerly VWS. The vortex tilts to the north-northeast with height. The modified-MHG (simplex) method center is denoted by the square. The vorticity centroid within the domain shown is denoted by the circle.

center. The new center is defined as the origin of the annulus within which the average tangential wind is maximized.<sup>2</sup> The annular geometry is especially well suited for mature TC applications because of minimal overlap with the data-sparse region in the eye. While the method is not restricted to the RMW scale, its application much beyond the RMW in individual passes will be compromised by poorer data coverage.

To illustrate the MHG method for Doppler-based center estimation without the complication of data gaps within the eyewall annulus, we first consider its application to a numerically simulated vortex in VWS. The dry dynamical core of the CM1 (Bryan and Fritsch 2002) was used to simulate the interaction of an initially barotropic vortex (i.e.,  $\text{RMW} = \text{constant}$ ) with westerly unidirectional VWS of  $8 \text{ m s}^{-1}$  over 10-km depth. Horizontal grid spacing was fixed at 2 km. The initial conditions were constructed to resemble Hurricane Guillermo's strength and horizontal scale ( $\text{RMW} = 30 \text{ km}$ ) during IOP1. A plan view of the vortex wind field at the lowest model level after the development of tilt is shown in Fig. 3. The sensitivity of the MHG method here and elsewhere was assessed by using  $\delta$  values ranging from 3 to 13 km. The 11-member population mean and standard deviation were used to evaluate the statistical significance of the center estimates. The mean center, located

6 km to the west and 4.3 km to the south of the grid origin, is indicated by the square symbol. The standard deviation in the  $x$  ( $y$ ) direction is 0.2 (0.3) km, indicating a relatively robust center estimate.

A further test of the method's robustness was made by adding observation-based azimuthal variance to the simulated wind field and then recomputing the mean centers. Wind analyses at 3-km altitude from passes 5 and 8 during IOP1 were chosen for their superior azimuthal coverage. The mean center with the pass 5 (8) variance is located 6.7 (5.9) km to the west and 4.6 (3.7) km to the south of the grid origin. In both cases, the standard deviations increased to 0.5–0.6 km. Thus, we are confident that even with realistic azimuthal variance present in the wind field, the method is capable of estimating the center within at least a horizontal grid cell of the “true” center noted above.

When the simulated centers are plotted at each model level (not shown), a left-of-shear tilt to the north-northeast is revealed. The bulging of vorticity contours to the south-southwest at the surface in Fig. 3 is a manifestation of the large-scale tilt asymmetry conveyed in previous studies through along-tilt vertical cross sections of (potential) vorticity (Jones 1995; RMG04; RMN10). Because the tilt asymmetry has radial structure that departs from that of a simple vortex displacement, center-finding methods that are scale-dependent will yield different center locations depending on their radial extent. For example, the vorticity centroid of the simulated vortex in Fig. 3 (denoted by the circle) falls close to the MHG-method center within the  $2 \times \text{RMW}$  radial domain shown but lies increasingly to the south-southwest of this center with progressive increases in the centroid computational domain. Ultimately, because the tilt asymmetry is radially confined, the vorticity centroid estimate is bounded. It is reasonable to view the tilt derived from the MHG method as reflective of the RMW-scale core.

The greatest barrier to accurate center estimation from the Doppler-based hurricane analyses is any irregular data distribution. The sparsest coverage is often found at the lowest levels (due to sea clutter removal) and uppermost levels (due to the small fractional area occupied by deep convection). As an example, Fig. 4 shows the horizontal wind speed at 1- and 2-km altitude for pass 7 during IOP1. At 2 km a contiguous data gap spanned  $\sim 70^\circ$  in the northwestern eyewall, whereas at 1 km a much larger gap approaching  $120^\circ$  was present within the same region. This type of gap structure, perpendicular to the flight track, is typical of single-aircraft FAST sampling and primarily a function of radar sensitivity.

To estimate reliable vortex centers when small data gaps are present, a modified MHG method was developed. The method is designed to minimize sensitivity to the estimated RMW, the subjectively prescribed annular

<sup>2</sup> When the minimization algorithm of Neldar and Mead (1965) is employed, as is done here, this method has been referred to as the “simplex method.”

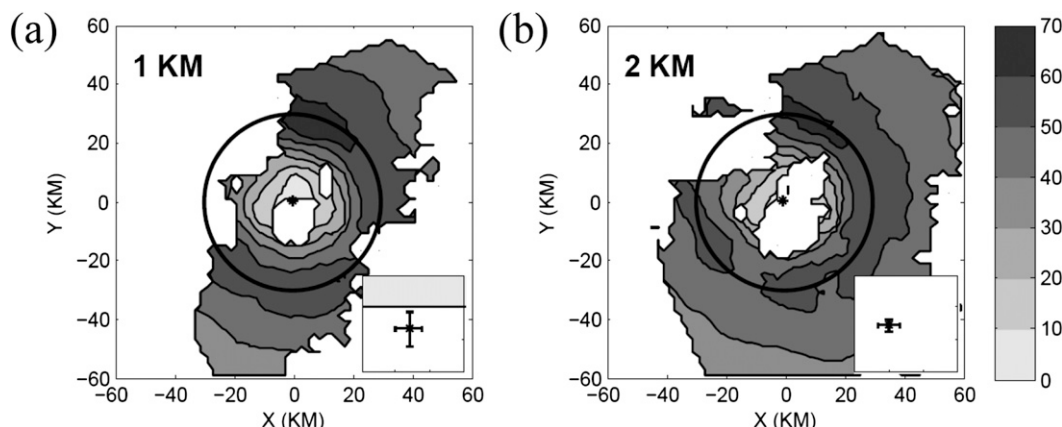


FIG. 4. Wind speed (shaded,  $\text{m s}^{-1}$ ) at (a) 1 and (b) 2 km from the 2225 UTC analysis during IOP1. Near the RMW (indicated by the circle) data gaps are most severe in the northwestern quadrant. The modified-MHG method center is denoted by the star. The insets show the standard deviations (bars in  $x$  and  $y$ ) associated with the center at each altitude within the same 3 km by 3 km domain. See the text for details on the center population used to compute the mean and standard deviation.

width (centered on the estimated RMW), the initial-guess vortex center, and the data resolution. As a result, vortex centers are identified only for cases with minimal data gaps, a well-defined RMW, and little sensitivity to the choice of annular width. Details of the method are provided in the appendix.<sup>3</sup> For the wind fields shown in Fig. 4, the method identified centers for all  $\delta$  values ranging from 3 to 13 km, and the mean center and standard deviation are shown. It is tempting to speculate that smaller standard deviations at 2 km are somehow related to the increased coverage. In fact when the gaps at 1 km were mapped to the wind field at 2 km, and the center population was recomputed, the change in standard deviation was small ( $\sim 0.1$  km). The mean center, however, shifted 0.75 km to the north. Thus, while the standard deviation may provide some measure of the robustness of a given center estimate, the presence of gaps could have a significant impact on the population mean. Quantifying this impact is not straightforward since the center mislocation likely depends on the proximity of gaps to mesoscale features of the eyewall.

At a minimum, we can quantify gap sizes near the eyewall for each pass during IOP1 and IOP2. Figure 5 shows the gap severity within a 20-km-wide annulus centered on the first-guess RMW (see the appendix) at 1- and 2-km altitude. The fraction of missing data points within

the annulus (Fig. 5a) reached as high as 55% at 1 km, but rarely exceeded 10%–15% at 2 km. Larger fractions were typically associated with analyses determined from a single fore/aft scanning radar. Because of a maximum gap fraction threshold of 35% (see the appendix), center estimates could not be made for several passes at 1 km and most passes above 9 km. The magnitude of the maximum contiguous azimuthal gap (Fig. 5b) directly impacts resolution of the low-wavenumber Fourier components. In particular, accurate estimation of wavenumber 1 requires a maximum gap of no more than  $90^\circ$ . This threshold was exceeded for many passes at 1 km (at some radial location), but was rarely exceeded at 2 km (only pass 7 during IOP2) due to superior data coverage. As a result, much of the subsequent discussion of pass-to-pass variability and time-mean structure in vortex tilt and local VWS use the 2-km centers as their low-level reference.

The tilt structure from 1 to 9 km, relative to the 2-km center, is shown in Fig. 6 for each wind analysis during IOP1 (Fig. 6a) and IOP2 (Fig. 6b). In this, and all subsequent analyses, fields are rotated such that the large-scale VWS consistently points due east. The 95% confidence intervals (in  $x$  and  $y$ ) for the mean center estimates are shown at 2 and 7 km (the layer chosen to represent the deep-layer vortex tilt). A mean center was plotted only if center estimates were identified for at least 7 of the 11 annular widths ( $\delta$  values). In all cases, identified centers at 2 and 7 km were sufficient to construct a mean. Outside this layer, the ability to represent the tilt structure varied on a pass-by-pass basis, as discussed above. Because the winds at adjacent vertical levels were not derived from completely independent data, level-to-level vertical tilt is not expected to exhibit a strong statistical significance.

<sup>3</sup> In Part I, gaps in the wind field where dual-Doppler data did not exist were filled by the variational method solution. Rather than use the reflectivity field to identify regions likely void of wind data, we have opted here to use “unfilled” wind analyses. This is a preferred method since gaps in the wind field are a function of both the distribution of reflectors and dual-Doppler beam geometry.

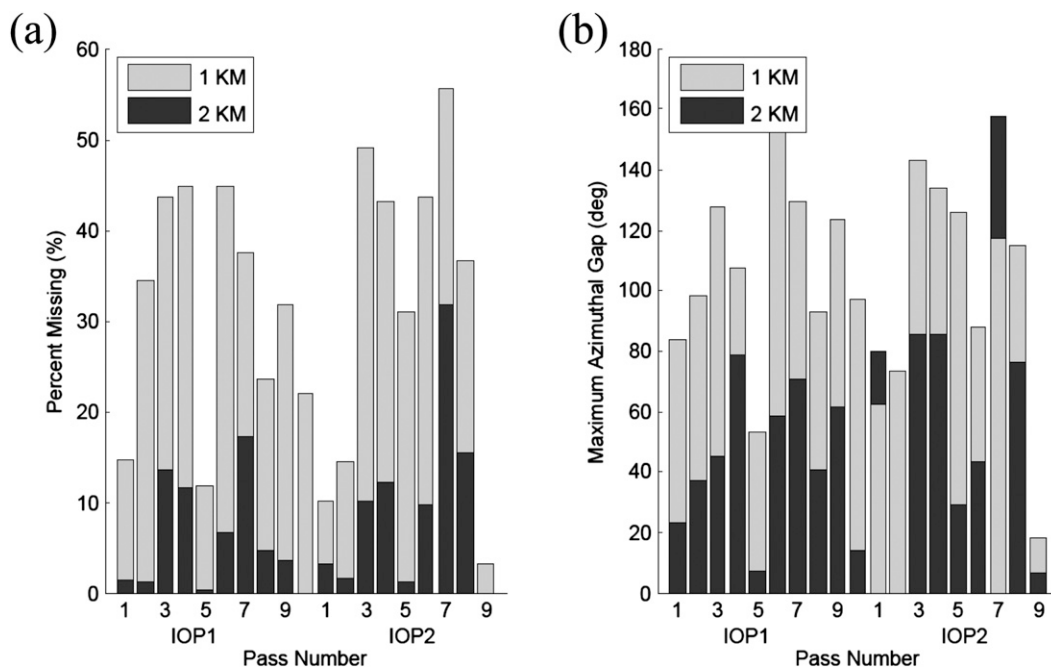


FIG. 5. Low-level gap severity quantified within a 20-km-wide annulus centered on the local RMW. (a) The percentage of missing data points at 1 and 2 km within this annulus is shown. The annulus was then split into 3-km radial bins, and the maximum contiguous azimuthal gap ( $^{\circ}$ ) between data points in any bin was computed. (b) The maximum gap for the annulus is shown.

However, the 2–7-km deep-layer tilt was statistically significant in all cases except pass 7 of IOP2. The tilt structure and its evolution are discussed further in section 3.

#### d. Quantification of local VWS in the TC core

Recent studies (e.g., Ritchie and Frank 2007) have suggested that the large-scale VWS impacting a TC may not be entirely accounted for by the shear of the synoptic flow in which the TC is embedded. The asymmetric flow generated by interaction of the baroclinic primary circulation of the vortex with the background PV field can also contribute to large-scale VWS. Ritchie and Frank showed that in the absence of synoptic flow, but with variable Coriolis parameter, deep-layer “beta shear” ranging in magnitude from 7 to  $12 \text{ m s}^{-1}$  can develop through this interaction. Temporal fluctuations in their large-scale shear estimate were attributed to variability of the simulated storm’s outflow layer. It is unclear whether this shear is represented in large-scale analyses like those used to derive the VWS estimate depicted in Fig. 1.

Because of the potential for a TC to interact with and modify its surrounding flow, the large-scale VWS shown in Fig. 1 may not necessarily reflect the shear “felt” by the TC core (e.g., Wong and Chan 2004; RMN10; Riemer and Montgomery 2011). Black et al. (2002) argued that deep convective bands outside the primary eyewall could

protect the core region from the effects of large-scale VWS by acting as barriers to relative flow. Defining the shear forcing of the vortex core region is particularly important if we wish to relate the findings of idealized studies (e.g., phase relationships) to the observations here. No well-established method for doing this exists at present, so we will continue to reference the large-scale SHIPS shear on the 500-km scale as our proxy for VWS forcing. Still, it is useful to examine more local measures of shear to understand potential deviations of VWS forcing from the large-scale estimate.

Here, the Doppler analyses were used to estimate local VWS within Guillermo’s core during both IOPs following a procedure similar to that described in Part I, but modified for consistency with our center estimation method. Details of the method are described in the appendix. At a given altitude during a given pass, an area-averaged storm-relative wind was computed only if a mean vortex center could be identified (i.e., those shown in Fig. 6). As before, because of the strict criteria on spatial coverage, the area-averaged wind at 1 km was often not available. Thus, individual hodographs for all passes (not shown) use 2 km as their low-level reference.

Figure 7 shows the time-averaged hodographs for IOP1 and IOP2 derived from the above method. The overall structure of the hodographs was similar for the two periods with the upper-level flow (relative to 2 km)



pointing in the direction of the large-scale VWS and an anticyclonic curvature with height. The anticyclonic curvature of the hodograph is similar to that observed in prior Doppler-based studies of TCs (Marks et al. 1992; Roux and Marks 1996; Reasor et al. 2000; Black et al. 2002). While level-to-level time-average differences were not significant, variations over deeper layers ( $>2$  km) were statistically significant.

The local deep-layer VWS is defined here as the difference between the area-averaged wind at 2- and 9-km altitude. The direction of the local VWS was consistent with that of the large-scale VWS during both periods, while the magnitude increased from  $8.5 \text{ m s}^{-1}$  during IOP1 to  $11.0 \text{ m s}^{-1}$  during IOP2 (although the increase was marginally significant at the 95% level). Recall that the large-scale VWS estimate from the SHIPS database (between 850 and 200 hPa) decreased in magnitude from 8.5 to  $4 \text{ m s}^{-1}$  over the same period. In studies of numerically simulated TCs, local shear computed using the center-relative flow at each height is generally less than the large-scale shear (e.g., RMN10). While we cannot rule out differences in the data and shear estimation methods, this atypical relationship between local and large-scale VWS may simply embody case-to-case variability. The complexity of real synoptic flows and vortex–environment interactions can conceivably contribute to departures from anticipated scale dependencies of VWS suggested by studies in which the imposed shear is uniform and for which the cyclonic vortex tilt is properly accounted.

### 3. VWS impacts on Guillermo's structure and evolution

In the absence of three-dimensional wind observations, tilting of the TC has been inferred primarily through satellite imagery. For example, Zehr (2003) quantified the pronounced deep-layer tilt evolution of a mature TC in VWS using animations of low- ( $\sim 1$  km) and high-altitude ( $\sim 15$  km) clouds from visible and infrared satellite imagery. During a period of increasing deep-layer VWS, the estimated vortex tilt increased to  $104^\circ$  and was oriented downshear. Although the VWS decreased by only a small amount in the 12-h period following its peak value, the tilt decreased by a factor of  $\sim 2$  and acquired a more left-of-shear orientation.

When TC tilt is more subtle (as observed during IOP1 and IOP2), such satellite-based techniques are likely to be ineffective. However, the Doppler-based method presented here, when applicable, provides core tilt estimates on the order of kilometers with relatively fine resolution in the vertical. In addition, when consecutive eyewall penetrations are performed, the tilt evolution can be documented over mesoscale periods.

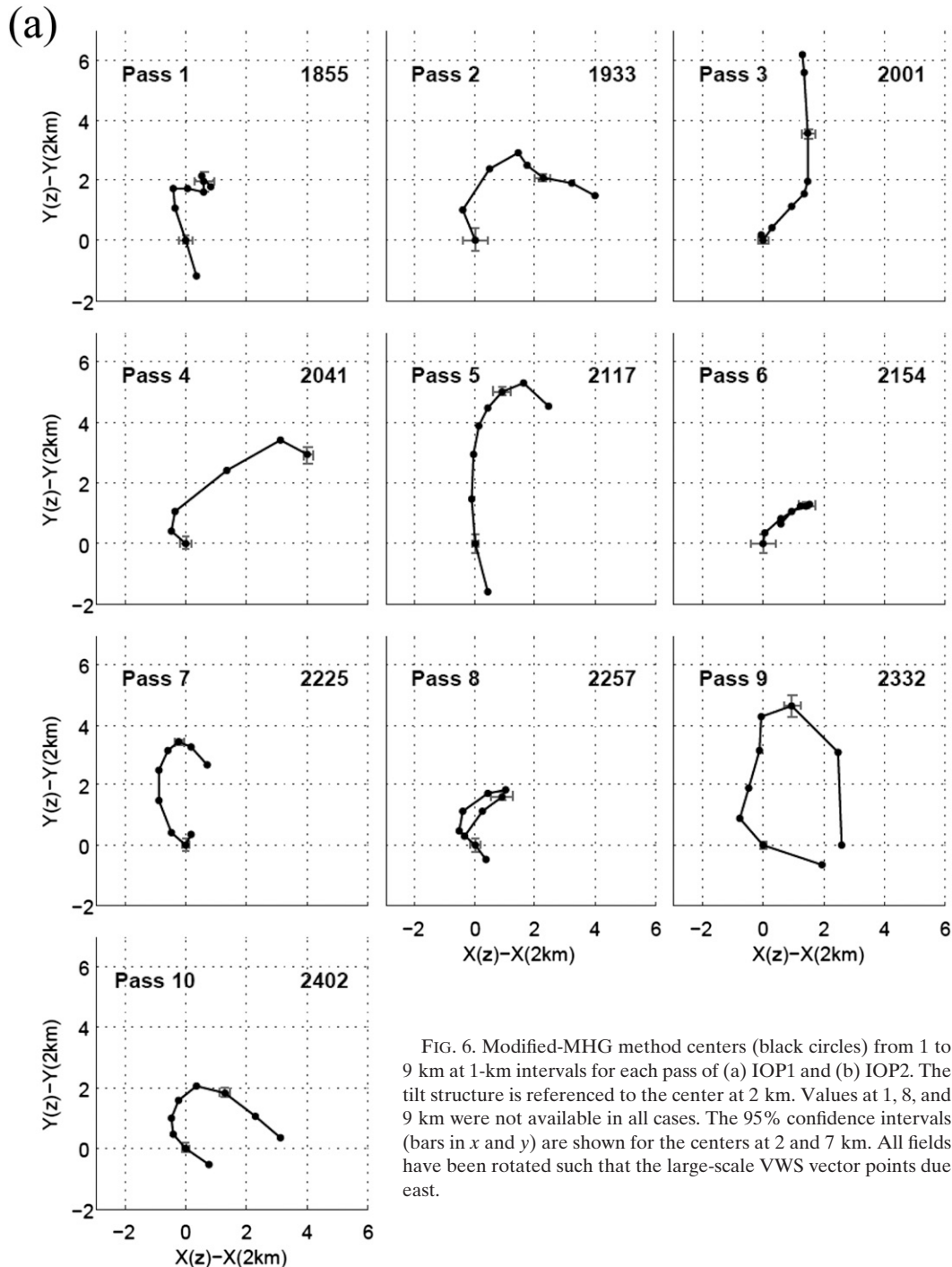
#### a. Observational support for a balanced-dynamical response to VWS forcing

A cursory examination of Guillermo's tilt evolution shown in Fig. 6 reveals a preference for deep-layer tilt oriented left of the large-scale VWS. Although fluctuations of tilt magnitude and direction occurred within the left-of-shear semicircle, it is instructive to consider first the time-averaged tilt structure and its relationship to other fields of interest. Figure 8 shows the time-averaged core tilt for IOP1 and IOP2. The 2–7-km tilt was significant during both periods. During IOP1 it was oriented  $63^\circ$  left of shear with a magnitude of 3.1 km. The tilt was oriented  $60^\circ$  left of shear during IOP2 with a smaller magnitude of 1.8 km. As a fraction of the RMW, these tilt values are  $<10\%$ , signifying a highly resilient vortex according to the MHG-method center estimates, which focus on the core. Differences in deep-layer tilt between IOP1 and IOP2 were marginally significant at the 95% level. The greatest difference in structure arose within the lowest 5 km where the vortex tilted left of shear during IOP1 and was more vertically aligned during IOP2.

The observation of sustained tilt left of shear, most prominently during IOP1, is physically significant since a similar orientation has been predicted by analytic models of vertically sheared hurricanes (RMG04) and simulated by moist numerical models (e.g., Braun and Wu 2007; Davis et al. 2008; RMN10). In the context of the linear treatment of RMG04, the  $90^\circ$  left-of-shear tilt exists as a stationary VRW solution associated with a shear-forced resilient barotropic vortex. The potential impact of increasing baroclinicity on tilt structure (in unidirectional VWS) was suggested by Jones (2000), and may include a transition from more unidirectional tilt profiles to anticyclonically curved profiles like those of Fig. 8. Further work is needed to better relate the vortices of idealized studies to those presented here.

In dry idealized studies of hurricanes in VWS, the vortex kinematic and thermodynamic structures are well described by balanced dynamics (Jones 1995; RMG04). As the PV of the vortex is vertically tilted, a balanced thermal asymmetry develops with anomalously cold (warm) potential temperature located downtilt (uptilt). In the quasi-steady  $90^\circ$  left-of-shear tilt orientation, cyclonically orbiting parcels would ascend (descend) adiabatically to the right (left) of the tilt direction, resulting in a region of ascent fixed to the downshear direction. Whether such a balanced-dynamical framework pertains to the moist TC vortex remains an open question at present (e.g., Frank and Ritchie 2001; RMG04; Braun et al. 2006; Davis et al. 2008; RMN10).

Although direct comparison between the theoretical predictions of idealized models and limited observational



datasets is generally a challenge, it is useful to document those fields that most effectively point to the underlying mechanisms highlighted in prior work. The first is the time-averaged wavenumber-1 vertical motion asymmetry (Fig. 9). As summarized in Davis et al. (2008), quasi-balanced mesoscale lifting forced by the vortex–shear interaction defines the location of diabatic heating. For

sufficiently tilted baroclinic vortices, Jones (2000) found that the mesoscale lifting was maximized  $90^\circ$  to the right of the tilt direction and maintained this phase relationship as the tilt direction varied with altitude. Thus, the presence of a warm core did not, to leading order, alter the explanation for vertical motion development offered by Jones (1995), originally for initially barotropic vortices.

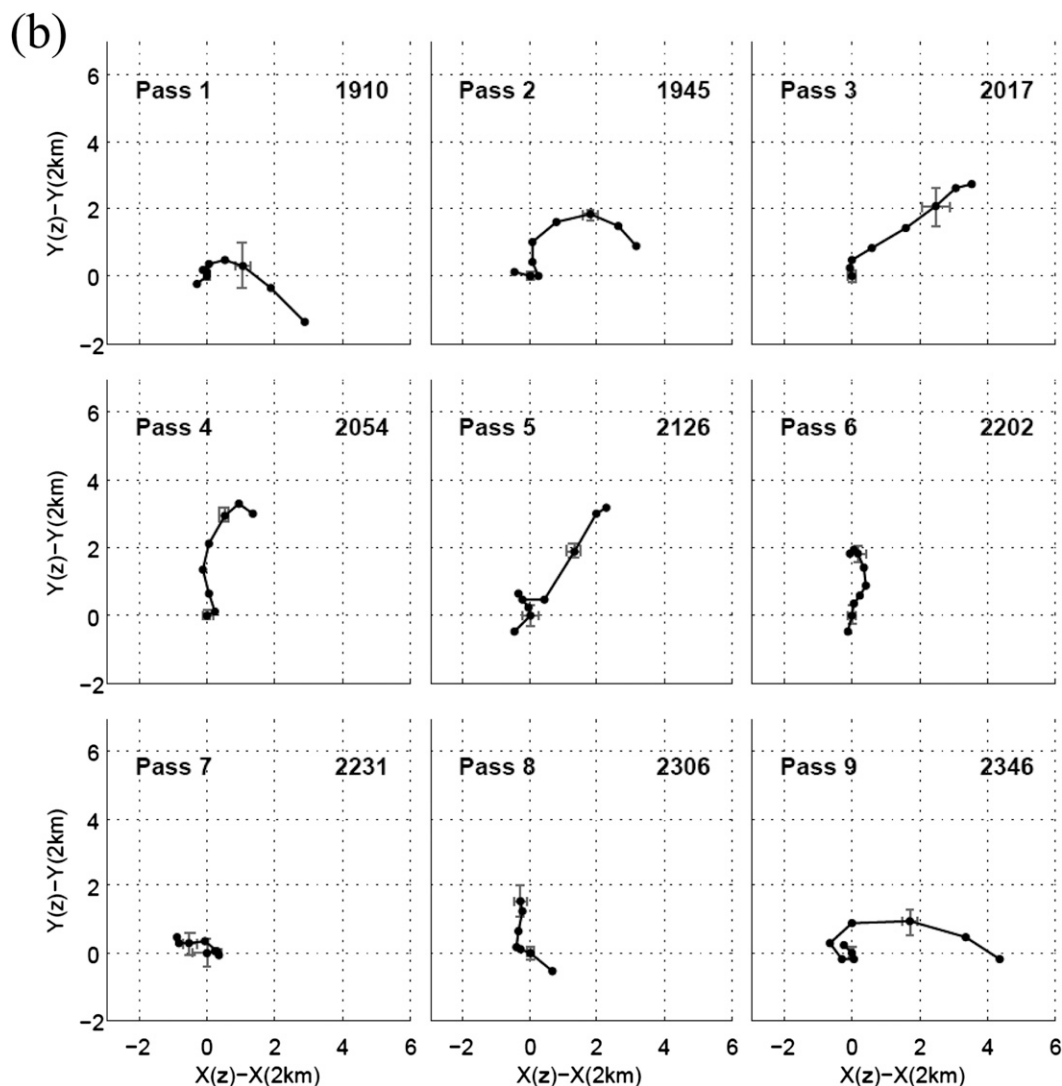


FIG. 6. (Continued)

Although not without exception, simulated sheared hurricanes in the literature typically exhibit maximum diabatic heating and ascent downtilt (e.g., Rogers et al. 2003; Braun et al. 2006; Wu et al. 2006; Davis et al. 2008). To motivate this preference for downtilt heating, Wu et al. (2006) invoked a vorticity balance argument similar to Willoughby et al. (1984) and Bender (1997), which assumes vorticity advection tends to oppose stretching of vorticity. According to this argument, storm-relative asymmetric inflow should coincide with enhanced convergence where the flow impinges upon the eyewall. At low-levels Wu et al. found the location of this enhanced mesoscale convergence generally coincided with the downtilt direction and served as a favored region for ascent.

At 5 km the envelope of wavenumber-1 ascent in the core region during IOP1 (Fig. 9a) and IOP2 (Fig. 9b)

was confined primarily to the downshear semicircle with peak values skewed  $\sim 40^\circ$  left of shear, or in this case, immediately to the right of the 2–7-km tilt. While this phase orientation is consistent with that found in a number of moist numerical studies, recall that the eyewall vertical velocity field was also modulated by rotating mesoscale vorticity asymmetries (see Fig. 17 in Part I). Vorticity asymmetries rotating through the broader envelope of shear-related convergence serve as focal points for strong convective bursts (Braun et al. 2006; Braun and Wu 2007). The vertical motion averaged over the short time windows of IOP1 and IOP2 ( $\sim 4$ – $5$  orbital periods at the RMW) will certainly reflect such internal processes not represented in current idealized models of the TC in shear. The relationship between vortex tilt and convective asymmetry in observed TCs is further explored in

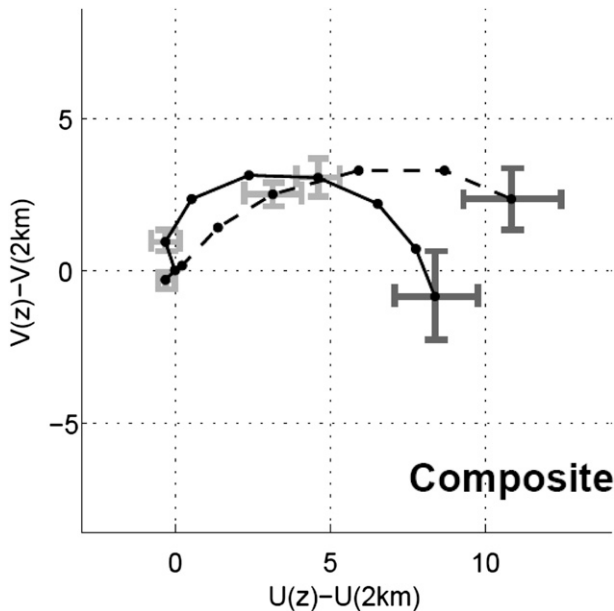


FIG. 7. Time-averaged local hodograph ( $\text{m s}^{-1}$ ) from 2 to 9 km at 1-km intervals for IOP1 (solid) and IOP2 (dashed). The hodographs are referenced to the area-averaged wind at 2 km. The 95% confidence intervals (bars in  $x$  and  $y$ ) are shown at 3, 6, and 9 km. See text for details on the Doppler-based storm-centered area averaging. All fields have been rotated such that the large-scale VWS vector points due east.

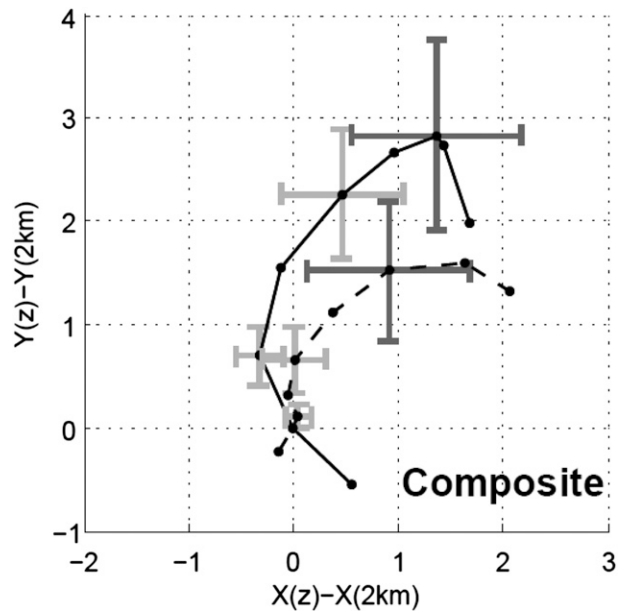


FIG. 8. Time-averaged tilt structure from 1 to 9 km at 1-km intervals for IOP1 (solid) and IOP2 (dashed). The tilt structure for each contributing pass is referenced to the center at 2 km. The 95% confidence intervals (bars in  $x$  and  $y$ ) are shown at 3, 5, and 7 km. All fields have been rotated such that the large-scale VWS vector points due east.

an upcoming multistorm examination of Doppler radar data.

More direct support for the balanced nature of the TC's response to shear forcing is made through analysis of the vorticity and thermodynamic fields. The wavenumber-1 relative vorticity asymmetry at 2 km is shown in Fig. 10. RMN10 noted a strong vorticity dipole in the inner core of their simulated hurricane in VWS that they attributed to a displacement of the vortex center from the origin of the cylindrical grid. In the present analysis, we centered the vortex at each height on the modified MHG-method center in an attempt to minimize this contribution to the wavenumber-1 asymmetry. The vorticity dipole observed here peaked near 20-km radius, well inside the radius of maximum symmetric vorticity gradient, and thus cannot be associated with a center displacement. A plausible explanation for the vorticity dipole is the amplification of vertical vorticity through enhanced vortex tube stretching left of shear in the convectively active region of the eyewall. Guillermo's symmetric vorticity structure satisfied the necessary conditions for barotropic instability during both IOP1 (see Figs. 11–12 in Part I) and IOP2 (not shown). In Part I cyclonically rotating vorticity asymmetries were documented (see Fig. 17), some possibly generated in association with this instability. The positive asymmetric

vorticity values were particularly large within the left-of-shear semicircle and often located cyclonically downstream of the updraft peaks.

The vorticity asymmetry within Guillermo's vortex skirt (beyond  $\sim 30$ -km radius at 2 km) surrounding the dipole is anticipated to reflect the large-scale tilt of the vortex. During IOP1, the vorticity asymmetry in the skirt was oriented in a manner consistent with the left-of-shear tilt at 2 km identified in Fig. 8. During IOP2, when the low-level vortex was only slightly tilted left of shear, the tilt asymmetry was not as clearly defined, with spiraling vorticity bands surrounding the vorticity dipole. However, an envelope of positive (negative) vorticity was still observed right of shear (left of shear). Using a larger  $4\text{--}5 \times \text{RMW}$  domain, RMN10 showed a similar relationship between the vorticity centroid tilt and low-level vorticity asymmetry within the skirt.

According to balanced-dynamical arguments, a thermal asymmetry should coincide with the tilted (potential) vorticity structure. Inspection of an along-tilt vertical cross section of potential temperature from the simulated hurricane of Braun and Wu (2007; see their Fig. 10) suggests that the pattern of thermal asymmetry is sensitive to the center employed. Because of a displacement of the mid- to upper-tropospheric warm core in the

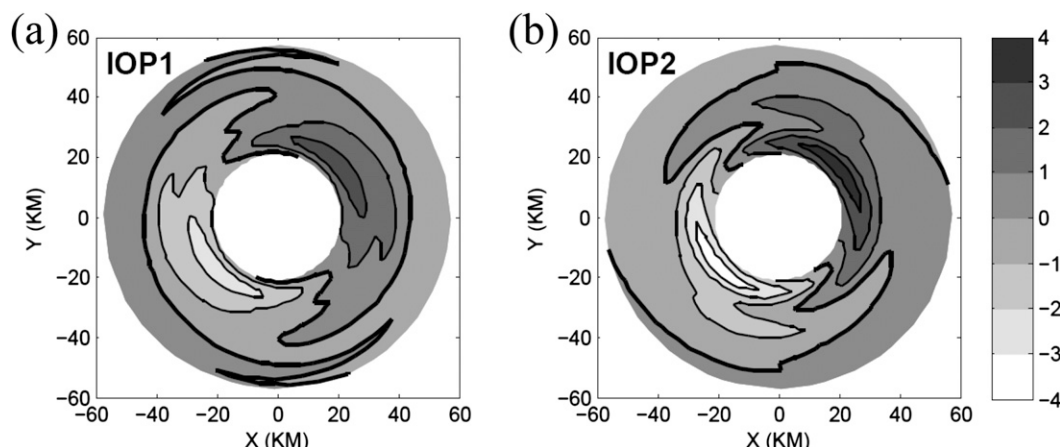


FIG. 9. Time-averaged wavenumber-1 vertical velocity asymmetry (shaded,  $\text{m s}^{-1}$ ) at 5 km for (a) IOP1 and (b) IOP2. The zero contour is indicated by the heavy line. All fields have been rotated such that the large-scale VWS vector points due east.

direction of tilt, the thermal asymmetry computed using the surface center at each altitude would exhibit positive values downtilt at upper levels. Using the local vortex center at each altitude would likely yield negative (positive) asymmetry values downtilt (uptilt) through a deep layer of the troposphere. In her analysis of the asymmetric thermal structure of dry baroclinic vortices in VWS, Jones (2000) centered the computation at each altitude on the local PV center. Indeed, the cold portion of the asymmetry was consistently downtilt through a deep layer of the vortex, even as the tilt rotated anticyclonically with altitude. We may infer from this result that, to leading order, the explanation for the thermal asymmetry of baroclinic TC-like vortices is unchanged from that provided by Jones (1995) in the barotropic

context. That is, the thermal asymmetry arises initially through adiabatic ascent/descent along the direction of tilt such that the vertically varying vortex wind field remains thermally balanced.

Figure 11 shows the potential temperature asymmetry at the 3- and 6-km flight levels derived from in situ aircraft measurements. The perturbation potential temperature field at each altitude was constructed by effectively removing mesoscale instrument wetting errors along each radial leg (following Eastin et al. 2002), and then computing and subtracting the azimuthal mean relative to the local center. Shown in Fig. 11 are leg segments with perturbation potential temperature in excess of +1 K (−1 K) to denote regions of warm (cold) asymmetry. During both IOP1 and IOP2, the orientation of the thermodynamic

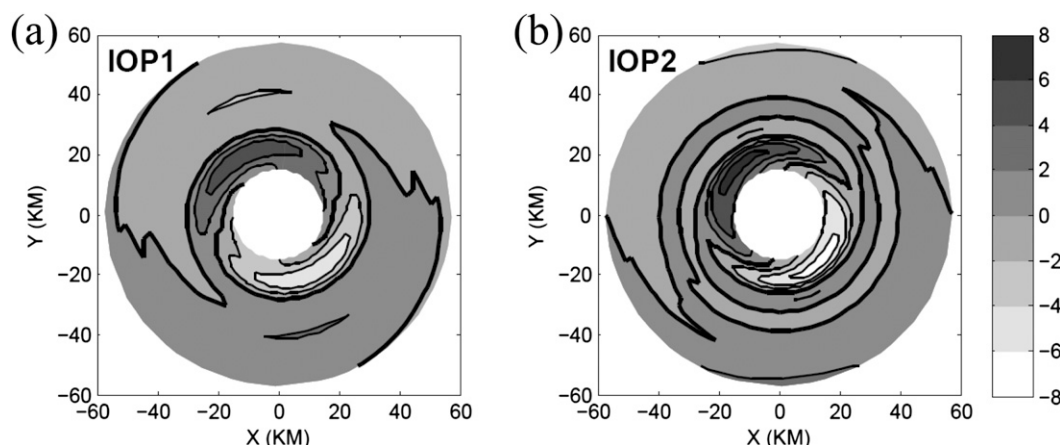


FIG. 10. Time-averaged wavenumber-1 vertical vorticity asymmetry (shaded,  $10^{-4} \text{ s}^{-1}$ ) at 2 km for (a) IOP1 and (b) IOP2. The zero contour is indicated by the heavy line. All fields have been rotated such that the large-scale VWS vector points due east.



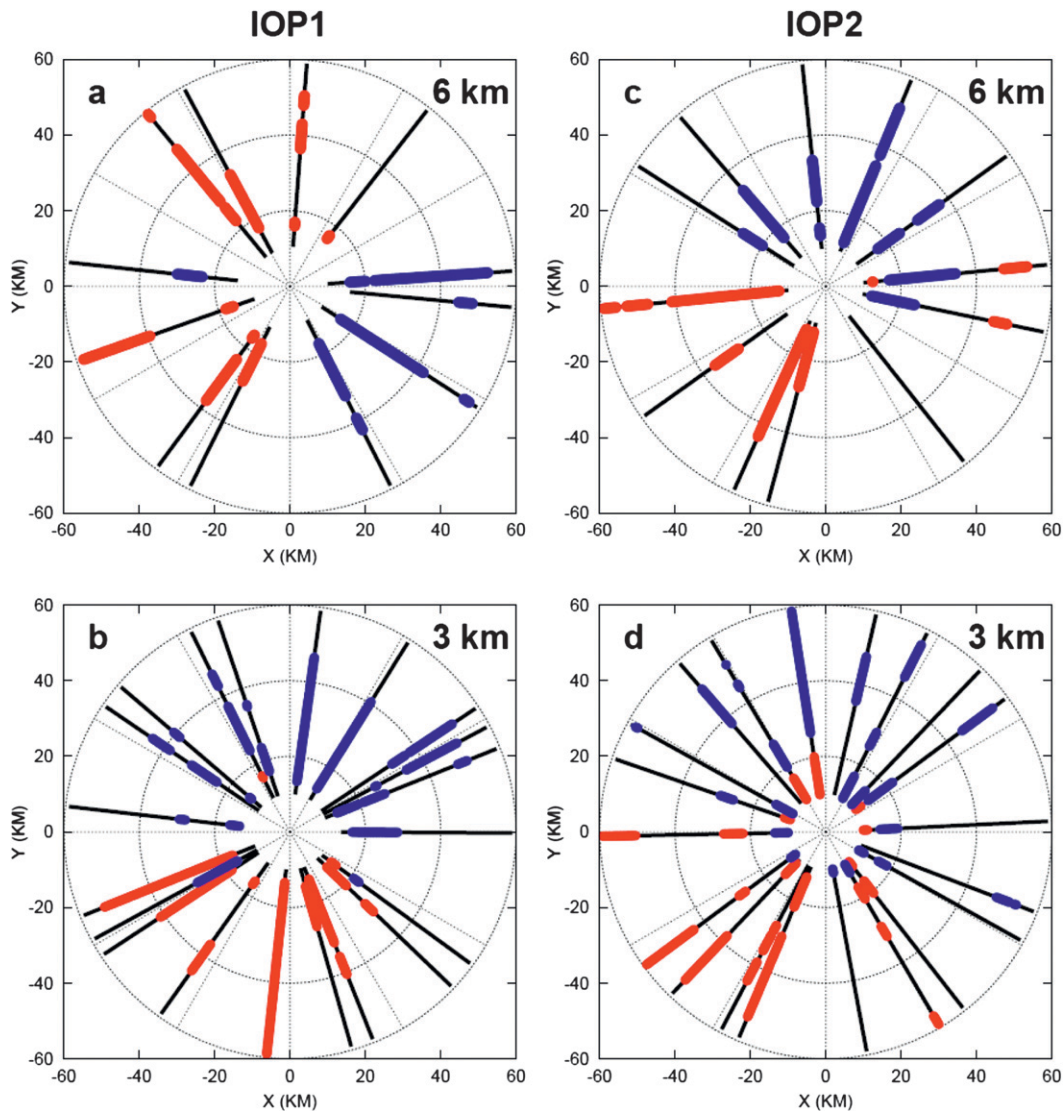


FIG. 11. Potential temperature asymmetry derived from aircraft flight-level measurements for (left) IOP1 and (right) IOP2. Red (blue) colors denote azimuthal perturbation potential temperatures that exceed +1 K (−1 K), which roughly corresponds to the mean standard deviation from the azimuthal mean radial profile. All fields have been rotated such that the large-scale VWS vector points due east.

asymmetry was consistent with the local vortex tilt.<sup>4</sup> At 3 km the cold anomaly coincided with the low-level, large-scale negative vorticity anomaly in the direction of tilt. The anticyclonic rotation of the thermodynamic pattern with altitude, most pronounced during IOP1, was broadly consistent with the anticyclonic rotation simulated by Jones (2000). Braun et al. (2006) showed a similar relationship between the direction of TC tilt and

the wavenumber-1 potential temperature asymmetry in their moist numerical simulations. They noted that despite latent heating downtilt, a mesoscale cold anomaly may still arise there if the adiabatic cooling exceeds the latent heating (Zhang et al. 2002) or anomalous adiabatic warming occurs through subsidence on the uptilt side.

#### *b. Observed evolution of TC tilt over mesoscale periods*

A uniqueness of the Guillermo dataset lies in its superior temporal resolution of mesoscale processes within the core region over a 4–5-h period. Of interest here is

<sup>4</sup> Perturbation equivalent potential temperatures computed in a similar manner (not shown) exhibit a qualitatively similar structure (but noisier) and orientation relative to the local vortex tilt.

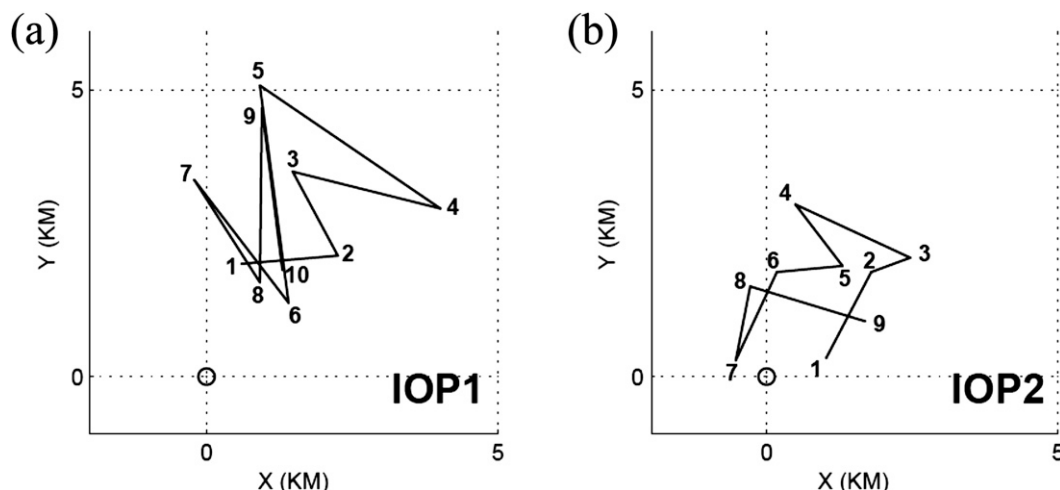


FIG. 12. Evolution of the 2–7-km tilt vector over a 4–5-h period during (a) IOP1 and (b) IOP2. The 2-km reference center is denoted by the open circle. The pass number is indicated by the numeric label. All fields have been rotated such that the large-scale VWS vector points due east.

the significance of the pass-to-pass evolution of vortex tilt and related asymmetry. In idealized studies of TC-like vortices in VWS, the imposed shear is typically held fixed either as a time-invariant forcing (RMG04) or through boundary conditions (e.g., Jones 1995; Frank and Ritchie 2001; Wong and Chan 2004; RMN10). The subsequent vortex tilt evolution ranges from cyclonic precession to quasi-steady tilting left of shear. During the periods encompassing IOP1 and IOP2, the large-scale VWS exhibited only small magnitude variations ( $<3 \text{ m s}^{-1}$ ; Fig. 1), and the pass-to-pass structure of the local VWS (not shown) did not depart significantly from the time average (see Fig. 7). Thus, it is reasonable to document the tilt evolution during both IOPs, and then qualitatively compare this evolution with the aforementioned numerical studies.

Figure 12 summarizes the 2–7-km tilt evolution (displayed in Fig. 6). During IOP1, the tilt vector was confined to the downshear-left quadrant and within  $\sim 45^\circ$  of the left-of-shear direction. The 7-km center underwent a seemingly erratic evolution relative to the 2-km center. However, a careful examination reveals some evidence for cyclonic looping, especially from pass 1 to 5, with increasing tilt magnitude. During IOP2, the tilt vectors were  $\sim 50\%$  weaker in magnitude but again exhibited a somewhat erratic cyclonic rotation. Interestingly, a cyclonic looping with alternating increasing and decreasing separation distance, ultimately converging to a steady-state tilt orientation  $90^\circ$  left of shear, was described by RMG04 for intrinsically resilient barotropic vortices subjected to VWS. RMN10 corroborated this type of vortex evolution in their idealized moist numerical simulations. Variations of this behavior of the deep-layer

tilt have also been documented in moist numerical case studies (e.g., Braun et al. 2006; Braun and Wu 2007; Davis et al. 2008), but often with departures from the theoretically predicted steady-state orientation of RMG04, similar to that observed here. As discussed above, the phase relationship between shear and tilt is subject to the definition of these quantities, which may exhibit non-unidirectional vertical structure. It should also be noted that temporal variations in large-scale VWS are not accounted for in existing theoretical models. Nevertheless, the qualitative agreement of simulated and observed tilt structure and evolution with current theoretical predictions continues to support the relevance of mechanisms intrinsic to the adiabatic dynamics.

Is the tilt evolution depicted in Fig. 12 significant? The pass-to-pass fluctuations in the deep-layer tilt derived from the modified MHG method may reflect some eyewall-scale variability unrelated to the tilting of the vortex core. At the same time, data coverage issues will contribute to center errors. Parallel numerical studies using the methods described here are needed to better define the significance of the tilt evolution over mesoscale periods. A large-scale tilt measure like the vorticity centroid would be better suited to addressing the tilt evolution since it is weighted more by asymmetry within the skirt and, thus, somewhat less sensitive to mesoscale features of the eyewall. Data coverage in individual analyses may be too sparse within the skirt region, however, to provide meaningful vorticity centroid estimates. Regardless of whether the evolution from one pass to the next is significant, the persistent tilt of the vortex left of the deep-layer shear agrees with predictions of analytic studies (RMG04) and the findings of moist numerical

simulations (Braun et al. 2006; Braun and Wu 2007; Davis et al. 2008; RMN10).

Differences in tilt evolution between IOP1 and IOP2 were largely in magnitude as the azimuthal ranges of the tilt vectors were comparable. The analytic study of RMG04 did not directly address the sensitivity of steady-state tilt magnitude to the parameters of the problem (e.g., VWS magnitude, vortex strength, RMW, static stability, Coriolis parameter, vortex depth, and skirt vorticity gradient). A recent study (Reasor 2010) using the model of RMG04 initialized with barotropic versions of the IOP1 and IOP2 vortex profiles, and with reduced static stability within the eyewall region, was able to reproduce qualitative differences in the quasi-steady tilt. In particular, the IOP2 vortex was only slightly smaller, but more intense (maximum wind speed at 2 km was  $\sim 10 \text{ m s}^{-1}$  greater) than the IOP1 vortex, and such a change likely contributed to Guillermo's enhanced resilience.

#### 4. Conclusions

As efforts to improve and validate operational TC model forecasts increase, the need for observational reference points exists. Observational documentation of VWS impacts upon the kinematic and thermodynamic structure of TCs has largely focused on the relationship between shear and vertical motion, with little attention paid to the significance, both physical and statistical, of the tilt structure (Marks et al. 1992; Reasor et al. 2000; Part I). In light of recent numerical studies of the relationship between VWS and TC intensity change (RMN10; Riemer and Montgomery 2011), the need for observational studies directed toward developing a complementary set of diagnostics is evident. Such diagnostics, including low-wavenumber analyses of the kinematic and thermodynamic fields, would form the basis for a comprehensive approach to addressing issues of TC resilience and intensity change in VWS from an observational perspective.

In this study we have presented a revised methodology for TC center and local vertical wind shear estimation with enhanced quality control and quantification of statistical significance from Doppler-based composite analyses. Radar and flight-level data collected during two missions into Hurricane Guillermo were used to demonstrate the utility of the method and diagnostics. The greatest challenge to documenting the TC vertical tilt from typical radar analyses is the irregular (and limited) data coverage provided by a single fore/aft scanning radar. Here, the addition of a second track-normal-scanning radar alleviated this problem in some cases. An optimal scanning strategy for future similar studies should employ two fore/aft scanning radars simultaneously sampling

the TC core along orthogonal radials. Nevertheless, the deep-layer tilt estimates from most of the 19 passes showed statistical significance and, more importantly, a relationship to the large-scale, deep-layer VWS consistent with analytic studies (RMG04) and moist numerical simulations (Braun and Wu 2007; Davis et al. 2008; RMN10).

Figure 13 summarizes the relationships among the observationally based diagnostics discussed herein. During both IOPs, the deep-layer vortex tilt fluctuated within  $\pm 20^\circ$  of an orientation  $\sim 60^\circ$  left of the large-scale VWS. Because of the anticyclonic rotation of the tilt vector with height, the low-level vorticity asymmetry within the skirt (associated with the vortex tilt) was nearly orthogonal to the VWS. The small magnitude of the deep-layer tilt relative to the horizontal vortex scale is indicative of a highly resilient vortex. Consistent with a balanced-dynamical response of the TC to VWS forcing, the asymmetric thermal pattern was oriented along the direction of local tilt. A right-of-tilt convective modulation corresponding to the balanced mesoscale vertical motion pattern anticipated in adiabatic simulations (Jones 1995, 2000) was not easily discerned in this case. Peak values of the wavenumber-1 component of vertical motion in the eyewall were more closely aligned downtilt and appeared to be influenced by deep convective bursts modulated by vorticity asymmetries rotating through the downshear-left quadrant.

With the addition of data from the second IOP, we were able to contrast the tilt structure and evolution between periods of rapid intensification in moderate large-scale VWS (IOP1) and steady-state intensity in weaker VWS (IOP2). The primary change in structure was greater vertical alignment within the lower troposphere and an overall reduction in tilt in the 2–7-km layer. Weaker large-scale VWS and a much stronger vortex during IOP2 would support a more resilient vortex. However, the statistical significance of such tilt differences was only marginal in this case.

RMN10 recently proposed a link between VWS, vortex tilting, and intensity change. Direct comparison with their results cannot be effectively addressed here with the present data. Our domain, while it does extend into the vortex skirt, would likely need to be extended to  $3\text{--}4 \times \text{RMW}$  in radial scale to verify the modulation of uptilt convection beyond the eyewall that is central to their weakening mechanism. Additionally, the available thermodynamic observations limit comparison of Guillermo's structure and environment to that of their simulated TC. Interestingly, the few observations suggest that regions of active convection may play a larger role in modulating the mesoscale thermodynamic structure of the storm than hypothesized. In particular, Eastin et al.

### Kinematic/Thermodynamic Structure of an Observed TC in VWS

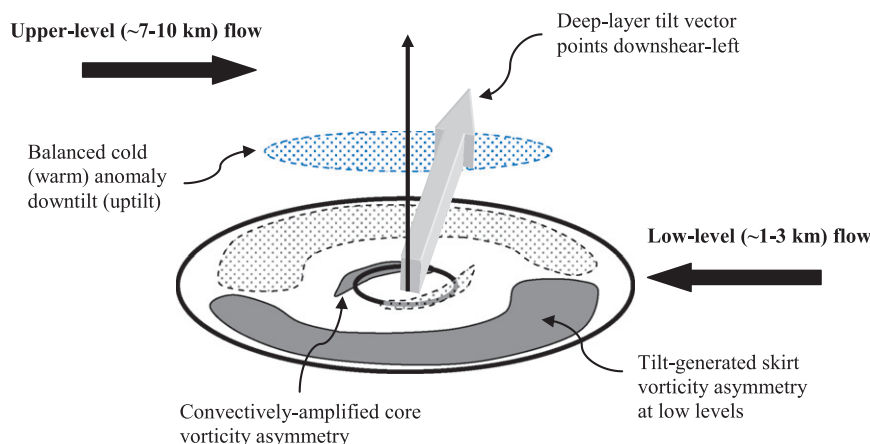


FIG. 13. Schematic illustration of Hurricane Guillermo's interaction with environmental VWS. In the quasi-steady tilt configuration, the tilt vector rotates anticyclonically with height, yielding a deep-layer, downshear-left tilt. Wavenumber-1 vorticity asymmetry in the vortex skirt is generated through tilting of the TC. Consistent with a balanced-dynamical evolution of the shear-forced TC, a cold (warm) anomaly develops downtilt (uptilt). To facilitate visualization of the entire schematic, the uptilt warm anomaly is not shown. A large-amplitude vorticity dipole is generated in the core through amplification of vertical vorticity in the convectively active downshear-left quadrant.

(2005) showed that the majority of midlevel downdrafts were located within or just downwind of active convection in the upshear eyewall and rainbands, but with no clear relationship between either VWS or vortex tilt and the local thermodynamic perturbations associated with the downdrafts. Sitkowski and Barnes (2009) showed near-surface cool pools, while located left of shear, were beneath or radially inside active rainbands. In contrast, the thermodynamic modification in RMN10 occurred well away from or radially outside active convection.

Ultimately, differences in the physical scenarios depicted here and simulated, for example, by RMN10 must be considered when testing intensity change hypotheses. Guillermo was a rapidly intensifying storm in gradually increasing VWS of  $8.5 \text{ m s}^{-1}$  during IOP1. The impacts documented by RMN10 after the instantaneous application of VWS were less pronounced at such lower shear values, and were minimal once the vortex realigned. From the perspective of internal core processes, the dynamic stability of the TC profile in the RMN10 study during most of the simulated evolution in VWS may have limited the degrees of freedom by which the vortex could counter downward transports of low equivalent potential temperature air into the boundary layer within the vortex skirt. The active exchange between Guillermo's eye and eyewall [documented in Part I for IOP1 and Eastin et al. (2005) for IOP2] could have provided the necessary "turbocharge" to support such a

rapid intensification (Persing and Montgomery 2003; Cram et al. 2007). In an upcoming paper we will address Guillermo's eye–eyewall exchange in more depth. The competing roles of inhibitive and supportive mechanisms for intensity change require further study.

Future works will expand this single case analysis to include a large database ( $>150$  individual eyewall passes) of Doppler radar analyses from NOAA/Aircraft Operations Center (AOC)–Hurricane Research Division (HRD) flights over the past two decades. By compositing cases relative to the deep-layer VWS, we hope to further establish the structural relationships described herein and to quantify the sensitivities of observed hurricane tilt and asymmetry to the VWS strength and vortex profile. In the last 2–3 years increased radial coverage has been emphasized during NOAA/AOC–HRD flights, permitting partial resolution of the vortex skirt out to 200-km radius. Portions of this database have recently been applied to a composite analysis of TC symmetric structure (Rogers et al. 2012). Preliminary results from shear-relative composites of radar-observed TCs support the case study findings here and will be reported in a forthcoming publication.

*Acknowledgments.* We thank Jessica Fieux who manually edited the Doppler radar data for IOP2 as part of her M.S. thesis project at Florida State University. We would also like to thank John Kaplan and John Gamache for their helpful comments on an earlier version of this



manuscript, and Rob Rogers and Sylvie Lorsolo for stimulating discussions. This work was originally supported by NSF Grants ATM-0514199 and ATM-0652264. Finally, we thank Michael Riemer and one anonymous reviewer for their insightful comments that helped improve the presentation and discussion of these results.

## APPENDIX

### Modified-MHG Method and Local Shear Estimation for “Gappy” Datasets

The MHG method for TC center estimation using Doppler radar analyses seeks to maximize the average tangential wind within an annulus of prescribed width  $\delta$ . The origin of the annulus that accomplishes this is identified as the vortex center. The central radius is typically chosen to coincide with a best-guess RMW. Because the eyewall slopes outward with height in a typical TC, the center-finding described below is applied at each altitude separately using the local RMW. In the absence of gaps, application of the simplex maximization algorithm (Neldar and Mead 1965) is straightforward. In the presence of data gaps, additional steps are required to ensure statistical significance of the results. These steps are discussed below in a generalized presentation of the modified-MHG method.

At each altitude, the Doppler wind analysis is assessed for its capacity to yield a meaningful center estimate. First, a reliable RMW must be determined. Data are binned into radial intervals about the grid origin (which coincides with an interpolated NHC best-track center). If the maximum contiguous azimuthal gap exceeds  $120^\circ$  within a radial bin, an azimuthal mean tangential wind is not computed there. The resulting radial profile is used to identify the first-guess RMW. Second, the RMW robustness is checked by computing additional RMW estimates using a narrow spectrum of radial bin widths. If the resulting spread exceeds 1.5 times the horizontal spacing of the analysis, a robust RMW cannot be determined, and no center is computed at that altitude. Third, the areal fraction of missing data (or gaps) within the eyewall region is assessed. If this fraction exceeds 35% within a 20-km-wide annulus centered on the RMW (chosen from the above population as that which yields the peak azimuthal mean tangential wind), no center is computed at that altitude. Otherwise, a population of center estimates is obtained using the simplex algorithm with slight variations in the annulus width and central radius. If the difference between the maximum and minimum center displacements exceeds approximately twice the horizontal spacing of the analysis, the method is not deemed robust and no center is computed.

If the conditions are met for a meaningful application of the MHG method, the simplex algorithm is performed for a population of  $\delta$  values ranging from 3 to 13 km. For each  $\delta$  value the central radius and initial-guess center used as input to the algorithm are varied over a range of  $\text{RMW} \pm 1$  km and  $\pm 1$  grid cell of the origin, respectively. For a given central radius, centers are discarded that fall outside one standard deviation of the mean. A mean center and mean annulus-average tangential wind is computed from the remaining centers. Over the range of central radius values, the mean center that yields the maximum annulus-average tangential wind is defined as the vortex center for that  $\delta$  value. A final quality control of the tilt profile is performed, flagging centers at altitudes where jumps in RMW or center location from level to level exceed the mean difference plus 1.5 times the standard deviation. Center values are linearly interpolated from adjacent levels to those altitudes where a center could not be determined or was flagged. The final vertical profile is then smoothed with a three-point triangular filter. A mean center and standard deviation are computed at those altitudes having at least seven nonflagged centers from the  $\delta$ -value population.

Similar to the center estimates, the local hodograph of area-averaged wind can be extremely sensitive when data gaps are present. To compute an area-averaged wind at a given altitude, first, a reliable center estimate must exist. Area-averaging within a cylindrical domain about the local center approximately “removes” the vortex flow. If the data distribution is biased toward one side of the storm (e.g., as a result of a pronounced asymmetry in convection and reflectors), then it may not be possible to adequately remove the vortex. Thus, the area average is restricted to an annular region within which the maximum contiguous azimuthal gap at each radius is less than  $90^\circ$ . Within this annulus the symmetric vortex component is explicitly removed before the area integration of Cartesian wind components. If the averaging annulus is too narrow ( $< 5$  km wide), no area average is attempted. Following the threshold used for the tilt profile, large level-to-level jumps in the hodograph are flagged. The final hodograph for each center profile of the  $\delta$ -value population results from a similar linear interpolation and filtering of the profile. A population mean hodograph is computed at those altitudes having at least seven nonflagged members. The area-averaged wind at each altitude typically exhibits little sensitivity to the spread in center locations.

## REFERENCES

- Bender, M. A., 1997: The effect of relative flow on the asymmetric structure in the interior of hurricanes. *J. Atmos. Sci.*, **54**, 703–724.



- Black, M. L., J. F. Gamache, F. D. Marks, C. E. Samsury, and H. E. Willoughby, 2002: Eastern Pacific Hurricanes Jimena of 1991 and Olivia of 1994: The effect of vertical shear on structure and intensity. *Mon. Wea. Rev.*, **130**, 2291–2312.
- Braun, S. A., and L. Wu, 2007: A numerical study of Hurricane Erin (2001). Part II: Shear and the organization of eyewall vertical motion. *Mon. Wea. Rev.*, **135**, 1179–1194.
- , M. T. Montgomery, and Z. Pu, 2006: High-resolution simulation of Hurricane Bonnie (1998). Part I: The organization of eyewall vertical motion. *J. Atmos. Sci.*, **63**, 19–42.
- Bryan, G. H., and J. M. Fritsch, 2002: A benchmark simulation for moist nonhydrostatic models. *Mon. Wea. Rev.*, **130**, 2917–2928.
- Corbosiero, K. L., and J. Molinari, 2003: The relationship between storm motion, vertical wind shear, and convective asymmetries in tropical cyclones. *J. Atmos. Sci.*, **60**, 366–376.
- Cram, T. A., J. Persing, M. T. Montgomery, and S. A. Braun, 2007: A Lagrangian trajectory view on transport and mixing processes between the eye, eyewall, and environment using a high-resolution simulation of Hurricane Bonnie (1998). *J. Atmos. Sci.*, **64**, 1835–1856.
- Davis, C. A., S. C. Jones, and M. Riemer, 2008: Hurricane vortex dynamics during Atlantic extratropical transition. *J. Atmos. Sci.*, **65**, 714–736.
- DeMaria, M., 1996: The effect of vertical shear on tropical cyclone intensity change. *J. Atmos. Sci.*, **53**, 2076–2088.
- , M. Mainelli, L. K. Shay, J. A. Knaff, and J. Kaplan, 2005: Further improvements to the Statistical Hurricane Intensity Prediction Scheme (SHIPS). *Wea. Forecasting*, **20**, 531–543.
- Eastin, M. D., P. G. Black, and W. M. Gray, 2002: Flight-level instrument wetting errors in hurricanes. Part I: Observations. *Mon. Wea. Rev.*, **130**, 825–841.
- , W. M. Gray, and P. G. Black, 2005: Buoyancy of convective vertical motions in the inner core of intense hurricanes. Part II: Case studies. *Mon. Wea. Rev.*, **133**, 209–227.
- Emanuel, K. A., 1986: An air–sea interaction theory for tropical cyclones. Part I: Steady-state maintenance. *J. Atmos. Sci.*, **43**, 585–605.
- , 1991: The theory of hurricanes. *Annu. Rev. Fluid Mech.*, **23**, 179–196.
- Frank, W. M., and E. A. Ritchie, 2001: Effects of vertical wind shear on the intensity and structure of numerically simulated hurricanes. *Mon. Wea. Rev.*, **129**, 2249–2269.
- Gamache, J. F., 1997: Evaluation of a fully three-dimensional variational Doppler analysis technique. Preprints, *28th Conf. on Radar Meteorology*, Austin, TX, Amer. Meteor. Soc., 422–423.
- , F. D. Marks Jr., and F. Roux, 1995: Comparison of three airborne Doppler sampling techniques with airborne in situ wind observations in Hurricane Gustav (1990). *J. Atmos. Oceanic Technol.*, **12**, 171–181.
- Gray, W. M., 1968: Global view of the origin of tropical disturbances. *Mon. Wea. Rev.*, **96**, 669–700.
- Jones, S. C., 1995: The evolution of vortices in vertical shear. I: Initially barotropic vortices. *Quart. J. Roy. Meteor. Soc.*, **121**, 821–851.
- , 2000: The evolution of vortices in vertical shear. III: Baroclinic vortices. *Quart. J. Roy. Meteor. Soc.*, **126**, 3161–3185.
- , 2004: On the ability of dry tropical-cyclone-like vortices to withstand vertical shear. *J. Atmos. Sci.*, **61**, 114–119.
- Jorgensen, D. P., 1984: Mesoscale and convective-scale characteristics of mature hurricanes. Part II: Inner core structure of Hurricane Allen (1980). *J. Atmos. Sci.*, **41**, 1287–1311.
- Kaplan, J., and M. DeMaria, 2003: Large-scale characteristics of rapidly intensifying tropical cyclones in the North Atlantic basin. *Wea. Forecasting*, **18**, 1093–1108.
- Knaff, J. A., M. DeMaria, J. Kaplan, C. R. Sampson, and J. M. Gross, cited 2011: Improved statistical intensity forecast models. National Hurricane Center. [Available online at [http://www.nhc.noaa.gov/jht/05-07\\_proj.shtml](http://www.nhc.noaa.gov/jht/05-07_proj.shtml).]
- Kossin, J. P., and M. D. Eastin, 2001: Two distinct regimes in the kinematic and thermodynamic structure of the hurricane eye and eyewall. *J. Atmos. Sci.*, **58**, 1079–1090.
- Lawrence, M. B., 1999: Eastern North Pacific hurricane season of 1997. *Mon. Wea. Rev.*, **127**, 2440–2454.
- Mallen, K. J., M. T. Montgomery, and B. Wang, 2005: Reexamining the near-core radial structure of the tropical cyclone primary circulation: Implications for vortex resiliency. *J. Atmos. Sci.*, **62**, 408–425.
- Marks, F. D., Jr., R. A. Houze Jr., and J. F. Gamache, 1992: Dual-aircraft investigation of the inner core of Hurricane Norbert. Part I: Kinematic structure. *J. Atmos. Sci.*, **49**, 919–942.
- Merrill, R. T., 1988: Environmental influences on hurricane intensification. *J. Atmos. Sci.*, **45**, 1678–1687.
- Molinari, J., D. Vollaro, and K. L. Corbosiero, 2004: Tropical cyclone formation in a sheared environment: A case study. *J. Atmos. Sci.*, **61**, 2493–2509.
- , P. Dodge, D. Vollaro, K. L. Corbosiero, and F. D. Marks Jr., 2006: Mesoscale aspects of the downshear reformation of a tropical cyclone. *J. Atmos. Sci.*, **63**, 341–354.
- Neldar, J. A., and R. Mead, 1965: A simplex method for function minimization. *Comput. J.*, **7**, 308–313.
- Persing, J., and M. T. Montgomery, 2003: Hurricane superintensity. *J. Atmos. Sci.*, **60**, 2349–2371.
- Reasor, P. D., 2010: Sensitivity of hurricane tilt evolution to outer-core profile. Preprints, *29th Conf. on Hurricanes and Tropical Meteorology*, Tucson, AZ, Amer. Meteor. Soc., 16C.7. [Available online at [http://ams.confex.com/ams/29Hurricanes/techprogram/paper\\_169060.htm](http://ams.confex.com/ams/29Hurricanes/techprogram/paper_169060.htm).]
- , and M. T. Montgomery, 2001: Three-dimensional alignment and corotation of weak, TC-like vortices via linear vortex Rossby waves. *J. Atmos. Sci.*, **58**, 2306–2330.
- , —, F. D. Marks Jr., and J. F. Gamache, 2000: Low-wavenumber structure and evolution of the hurricane inner core observed by airborne dual-Doppler radar. *Mon. Wea. Rev.*, **128**, 1653–1680.
- , —, and L. D. Grasso, 2004: A new look at the problem of tropical cyclones in vertical shear flow: Vortex resiliency. *J. Atmos. Sci.*, **61**, 3–22.
- , M. Eastin, and J. F. Gamache, 2009: Rapidly intensifying Hurricane Guillermo (1997). Part I: Low-wavenumber structure and evolution. *Mon. Wea. Rev.*, **137**, 603–631.
- Reynolds, R. W., and T. M. Smith, 1993: An improved real-time global sea surface temperature analysis. *J. Climate*, **6**, 114–119.
- Riemer, M., and M. T. Montgomery, 2011: Simple kinematic models for the environmental interaction of tropical cyclones in vertical wind shear. *Atmos. Chem. Phys.*, **11**, 9395–9414.
- , —, and M. E. Nicholls, 2010: A new paradigm for intensity modification of tropical cyclones: Thermodynamic impact of vertical wind shear on the inflow layer. *Atmos. Chem. Phys.*, **10**, 3163–3188.
- Ritchie, E. A., and W. M. Frank, 2007: Interactions between simulated tropical cyclones and an environment with a variable Coriolis parameter. *Mon. Wea. Rev.*, **135**, 1889–1905.
- Rogers, R., S. Chen, J. Tenerelli, and H. Willoughby, 2003: A numerical study of the impact of vertical shear on the distribution

- of rainfall in Hurricane Bonnie (1998). *Mon. Wea. Rev.*, **131**, 1577–1599.
- , S. Lorsolo, P. Reasor, J. Gamache, and F. Marks, 2012: Multi-scale analysis of tropical cyclone kinematic structure from airborne Doppler radar composites. *Mon. Wea. Rev.*, **140**, 77–99.
- Roux, F., and F. D. Marks Jr., 1996: Extended velocity track display (EVTD): An improved processing method for Doppler radar observations of tropical cyclones. *J. Atmos. Oceanic Technol.*, **13**, 875–899.
- Schecter, D. A., M. T. Montgomery, and P. D. Reasor, 2002: A theory for the vertical alignment of a quasigeostrophic vortex. *J. Atmos. Sci.*, **59**, 150–168.
- Simpson, R. H., and H. Riehl, 1958: Mid-tropospheric ventilation as a constraint on hurricane development and maintenance. *Proc. Tech. Conf. on Hurricanes*, Miami, FL, Amer. Meteor. Soc., D4.1–D4.10.
- Sitkowski, M., and G. M. Barnes, 2009: Low-level thermodynamic, kinematic, and reflectivity fields of Hurricane Guillermo (1997) during rapid intensification. *Mon. Wea. Rev.*, **137**, 645–663.
- Wang, Y., and G. J. Holland, 1996: Tropical cyclone motion and evolution in vertical shear. *J. Atmos. Sci.*, **53**, 3313–3332.
- , M. Montgomery, and B. Wang, 2004: How much vertical shear can a well-developed tropical cyclone resist? Preprints, *26th Conf. on Hurricanes and Tropical Meteorology*, Miami, FL, Amer. Meteor. Soc., 100–101.
- Willoughby, H. E., F. D. Marks, and R. J. Feinberg, 1984: Stationary and moving convective bands in hurricanes. *J. Atmos. Sci.*, **41**, 3189–3211.
- Wong, M. L. M., and J. C. L. Chan, 2004: Tropical cyclone intensity in vertical wind shear. *J. Atmos. Sci.*, **61**, 1859–1876.
- Wu, L., S. A. Braun, J. Halverson, and G. Heymsfield, 2006: A numerical study of Hurricane Erin (2001). Part I: Model verification and storm evolution. *J. Atmos. Sci.*, **63**, 65–86.
- Zehr, R. M., 2003: Environmental vertical wind shear with Hurricane Bertha (1996). *Wea. Forecasting*, **18**, 345–356.
- Zhang, D.-L., Y. Liu, and M. K. Yau, 2002: A multiscale numerical study of Hurricane Andrew (1992). Part V: Inner core thermodynamics. *Mon. Wea. Rev.*, **130**, 2745–2763.